High-Fidelity Simulations of Propeller-Wing Interactions in High-Lift Conditions

Pinto Ribeiro, A.; Duivenvoorden, R.R.; Martins, Diogo

DOI
10.2514/6.2023-3541

Publication date
2023

Document Version
Final published version

Published in
AIAA AVIATION 2023 Forum

AIAA AVIATION Forum
12-16 June 2023, San Diego, CA and Online
AIAA AVIATION 2023 Forum

10.2514/6.2023-3541

High-Fidelity Simulations of Propeller-Wing Interactions in High-Lift Conditions

André F. P. Ribeiro*
Dassault Systemes GmbH, Stuttgart, Germany
Delft University of Technology, Delft, The Netherlands

Ramon R. Duivenvoorden†
Delft University of Technology, Delft, The Netherlands

Diogo Martins‡
Dassault Systemes GmbH, Munich, Germany

The recent increased interest in distributed propulsion and electric vertical take-off and landing vehicles have made propeller wake interactions with the aircraft more relevant. The interaction between high-lift wings and propeller slipstreams are still not fully understood and several research efforts are being carried out to improve that knowledge. Lattice-Boltzmann, very large eddy simulations of a propeller-wing-flap configuration are conducted in this work. The simulations are validated with experimental data, with very good agreement of surface static pressure, surface shearlines, and wake total pressure. The complex separation patterns on the flap and their interaction with the slipstream of the propeller are well captured. The effects of grid resolution and laminar-to-turbulent transition are demonstrated. With the simulations validated, they are used to better understand the flow field of this configuration. We find that the angle of attack has a strong effect on how the slipstream is split over the wing, that the tip vortices wrap around the wing leading-edge instead of being cut by it, and that increased circulation stabilizes the tip vortices on the suction side, while making the tip vortices on the pressure side more unstable.

I. Introduction

With the recent boom in the electric vertical take-off and landing (eVTOL) market and the interest in hydrogen-powered short-haul aircraft, distributed propulsion has become an important academic and industrial topic. Several institutions are investigating aircraft with large numbers of propellers on their wings, such as the NASA X-57 [1]. Extensive fundamental studies on propeller installation effects have been conducted at the Delft University of Technologu (TUD), focusing on tip mounted propellers [2], interaction between multiple propellers [3], distributed propulsion [4] and propeller-wing interaction in high-lift conditions [5]. The latter provides a challenging case for numerical methods, with highly complex and interactive flow fields featuring dominant viscous effects.

In this work, recent experimental results from TUD [5] are used to validate numerical simulations of interactions between a propeller and a wing with a deployed flap. The lattice-Boltzmann method (LBM) [6] is used as an alternative to the Navier-Stokes (NS) equations [7]. This method is particularly suited for high-fidelity simulations of wakes, as it offers low-dissipation characteristics equivalent to high order methods [8], while being orders of magnitude faster than traditional computational fluid dynamics (CFD) solvers [9].

II. Numerical Methods

In the last two decades, the LBM [10] has been growing in popularity as an alternative to the NS equations. The objective is the same: to have a description of the velocity and pressure fields over time, based on a certain mesh and timesteps. However, instead of using continuum mechanics as the foundation for describing fluid flow, statistical mechanics are used, considering the fluid as particles that interact with each other and with the boundary conditions.

*Senior Specialist, Aerospace Fluids, SIMULIA, andre.ribeiro@3ds.com, AIAA Member.
†PhD Candidate, Faculty of Aerospace Engineering, department of Flow Physics and Technology, AIAA Member.
‡Industry Process Specialist, Aerospace Fluids, SIMULIA.

We first need to consider that a particle can be in a certain spatial coordinate $\vec{x}$. Then, we consider that the particle has a certain velocity $\vec{c}$, which is not the fluid velocity. These quantities change as a function of time t. As dealing with individual particles quickly becomes too expensive, we instead work with the distribution function $f(\vec{x}, \vec{c}, t)$, which represents the probability that particles at position $\vec{x}$ and time t have the velocity $\vec{c}$. This can also be interpreted as the number of particles in a certain location and time that are travelling with a certain velocity. Fluid properties can be extracted from the moments of the distribution function. The Boltzmann equation describes the behavior of f:

$$\frac{\partial}{\partial t} f(\vec{x}, \vec{c}, t) + \vec{c} \nabla f(\vec{x}, \vec{c}, t) = C \tag{1}$$

where C is the collision operator, which defines how particles interact and is related to the fluid viscosity. This equation has similarities with the NS equations, with a time derivative of the main quantity as the first term, an advection component as the second term, and a viscosity term on the right side.

In LBM, besides space-time, which is discretized as in NS solvers, the particle velocities must also be discretized to obtain a method that can be computationally efficient. Particles can only travel in a finite number of directions and velocities $\vec{c}_i$. The choice of the discretization of the velocity space is a critical part of the LBM. In general, the fewer directions particles can travel to, the less physics are captured by the method and the more directions, the higher the computational cost. For isothermal, quasi-incompressible cases, particles only need to travel to adjacent cells for mass and momentum conservation to be achieved. A cost-effective option is to use the D3Q19 formulation, i.e., a 3D 19-states model. This means that particles can travel to 18 adjacent cells, or stay in their current cell. This is shown in Figure 1, where the circles denote the directions particles can travel in, for a lattice of cubic cells.

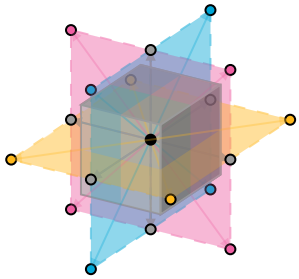

Fig. 1 Discretization of the velocity space into 19 vectors.

These assumptions lead to the lattice-Boltzmann equation:

$$f_i(\vec{x} + \vec{c}_i \Delta t, t + \Delta t) = f_i(\vec{x}, t) + C_i(\vec{x}, t) \tag{2}$$

where the subscript i denotes the discrete velocities that particles are assumed to be able to travel to and Δt is the timestep. As in the NS equations, a force term can be added to the lattice-Boltzmann equation, in order to simulate the effect of gravity, Coriolis forces, or other fields that affect the flow, and the eddy viscosity can be added to the fluid viscosity in C. Equation 2 can be interpreted as such: the particle density function for discrete $\vec{x}$, $\vec{c}$, t is computed based on two processes, the advection and the collision steps. In the advection step, a particle is streamed from one cell to another by $\vec{c}\Delta t$. One key factor of this step is that, with appropriate choices for $\vec{c}$ and Δt, no interpolation is needed to compute fluxes, in contrast to the advection of the NS equations. This makes this step very inexpensive, computationally, while also making it have little numerical dissipation. The collision step accounts for the interaction between particles with different velocities in the same cell. This is usually computed with the Bhatnagar–Gross–Krook (BGK) [11] approximation, which only depends on simple mathematics based on local quantities, again making it computationally inexpensive and suited for parallelization, unlike the Laplacian term in the NS equations.

Our LBM computations are conducted with PowerFLOW®, a commercial CFD code. It employs a k–ϵ RNG turbulence model [12] with a swirl model [13], which reduces the eddy viscosity in the presence of resolved flow structures, an approach called very large eddy simulation (VLES). A unique capability of PowerFLOW is in the handling of very complex geometry [14], with its Cartesian mesh being cut by surface elements, or surfels [15]. A sliding mesh [16] is used to rotate the propeller. Validations of the approach used here that are relevant to this work include vortical flows [17], rotors [18], tracks [19], wings in stall conditions [20], and a propeller-mounted high-lift wing [21].

III. Test Case Description

The geometry used in this work is a straight wing based on the NLF-Mod22(B) airfoil [22], with a nested chord $c = 300$ mm, a span of 1.248 m, and a Fowler flap with 30% of the full airfoil chord. The wing is equipped with a TUD-XPROP-S reference propeller [4, 23], with a diameter $D = 203.2$ mm and a blade pitch at 70% of the radius of 30°. The propeller is installed 173.5 mm ($\approx 0.858D$) from the leading-edge, with the axis of rotation angled 5° with respect to the wing chord line. The flow conditions are freestream velocity $U_\infty = 30$ m/s, resulting in $Re \approx 600{,}000$, and a propeller advance ratio of $J = U_\infty/(Dn) = 0.8$, where n is the rotational speed in rotations per second.

A. Experimental Setup

The experimental data used for validation in this paper were obtained in the Low Turbulence Tunnel at the TUD. The cross-section of the octagonal test section measures 1.25 m high by 1.8 m wide and is slightly divergent to compensate for the wall boundary layer. The wing was mounted vertically, clamped between both walls, with the flap attached the main element using 6 brackets. The main element of the wing model was tripped by a zigzag-strip, while the flap was left to transition naturally.

The experimental data set includes pressure tap measurements, total pressure in the wake plane, and oil flow visualizations. The pressure taps were located in two chord-wise rows positioned at $y = 0.7R$ on either side of the nacelle. A wake rake of total pressure probes on a traverse mechanism was used to capture total pressure in the wake, one chord downstream of the nested flap trailing-edge, with a resolution of 10 mm in spanwise and 3 mm in vertical directions. Oil flow visualization was achieved using a solution of UV-luminescent material in a light paraffin oil, taking images while wind was on after the oil had been allowed to transport sufficiently. Further details on the experimental setup are detailed in [5]. Table 1 summarizes the configurations and data points from the experiment which are considered for validation in this paper. Here, δ_f is the flap deflection angle, dx is the flap overlap with the main element, and ds is the gap between the flap and the main element leading-edge.

Table 1 Overview of experimental configurations used for validation.

δ_f [°]	ds [c]	dx [c]	U_∞ [m/s]	J [-]
0	-	-	30	0.8
15	0.02	0.08	30	0.8
30	0.03	0	30	0.8

Pressure tap measurements were taken at angles of attack α between -5 and 18° for the flap nested configuration, and up to 14° for the flap deployed configurations. Oil flow visualisations were taken for $\alpha = 0$ and 10° for the flap nested configuration, and $\alpha = 0$, 5, 8 and 10° for the flap deployed configurations. Wake rake measurements were taken at the same angles as the oil flow, with the exclusion of $\alpha = 5°$ for the flap deployed configurations.

B. Numerical Setup

Simulations are run with PowerFLOW 6-2021-R7, using the subsonic isothermal solver, as the freestream Mach number is 0.088 and the tip Mach number due to the propeller rotation is 0.35. A Cartesian mesh is used, with cubic cells ranging from 0.03 mm on the propeller blades leading-edges to 61 mm far from the wing. An average y^+ of 40 was used on the wing. A large refinement cylinder with cell size of 0.96 mm was placed around the propeller wake, to avoid numerical dissipation up to the experimental measurement plane. A refinement region, with cell size of 0.48 mm, was placed near the flap upper surface, to capture separation effects and the shear layer from the main element trailing-edge. A plane showing the mesh setup is shown in Fig. 2, where the outline of the sliding mesh interface, which is 10 mm from the blades and spinner, can also be seen.

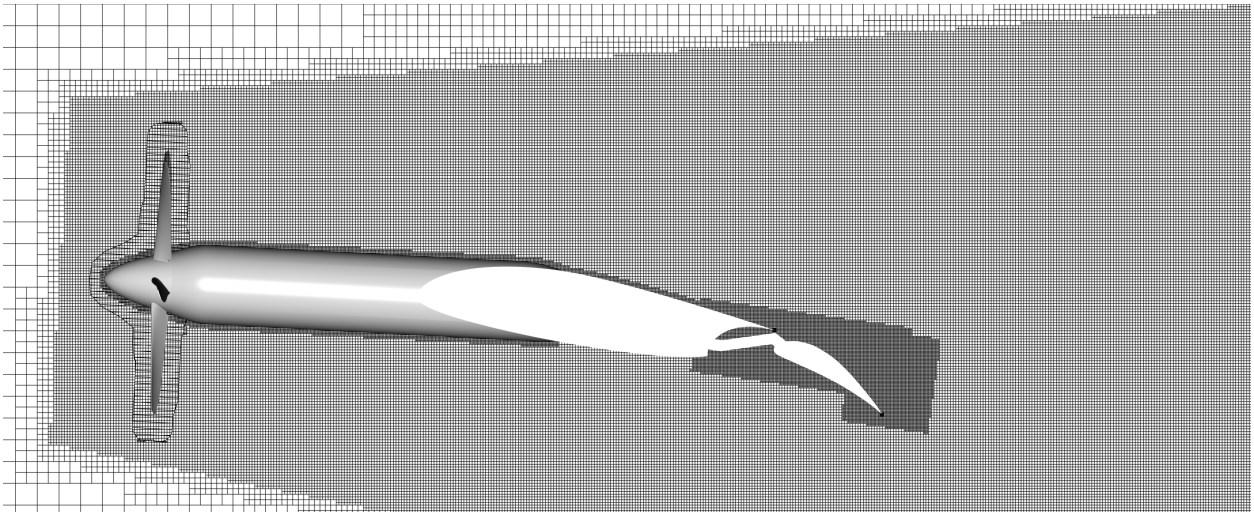

Fig. 2 Center plane of the wing showing the mesh used in the simulations. Every other line shown for clarity.

The mesh dimensions given in the previous paragraph are for the baseline mesh used throughout this study. This can also be referred to as the medium resolution cases. Two additional setups are used, to check for grid independence of the results. These are the coarse and fine cases, which have cells that are 1.25 times larger and smaller than the medium case, respectively. Due to the nature of the Cartesian mesh, that means that the ratio of the number of cells from coarse to medium and from medium to fine is about two.

The simulations are setup similar to previous works on wing sections [24, 25]. The wind tunnel walls are included to account for blockage effects, but are simulated as free slip walls. Hence the additional blockage effects due to the side walls boundary layers are neglected. These effects can be included if needed, but it is often challenging to do so exactly [26]. The side walls boundary layers effects on the wing root vortex are also neglected. Unless stated otherwise, the surfaces of the propeller and wing are modelled as fully turbulent. The boundary conditions used in the upstream and downwind faces of the numerical wind tunnel are a velocity inlet and a pressure outlet, respectively.

IV. Validation of Numerical Results

In this Section, we perform a thorough comparison with experimental data, before moving on to conducting a detailed analysis of the flow in Section V.

A. Propeller Thrust

The reference thrust coefficient of the TUD-XPROP-S propeller is $T_c = T/(q_\infty A) = 1.05$, where T is the thrust force, $q_\infty = 0.5\rho_\infty U_\infty^2$ is the freestream dynamic pressure, ρ_∞ is the freestream air density, and A is the propeller rotor plane area. This was measured for the isolated propeller at $\alpha = 0°$. We can use this as an approximate reference for our simulations and concurrently verify if the propeller thrust achieved in CFD is grid convergent. The values of T_c for the three resolutions simulated at $\delta_f = 30°$, $\alpha = 8°$ are shown in Table 2. The reason for this specific flap and wing angle settings are that we also use the same simulations to perform a resolution study on the wing aerodynamics (see Section IV.B), and this is the case with the most complex aerodynamics.

Table 2 Propeller thrust for different grid resolutions at $\delta_f = 30°$, $\alpha = 8°$ and experimental value for isolated propeller at $\alpha = 0°$.

Resolution	T_c
Coarse	1.032
Medium	1.039
Fine	1.042
Experiment	1.05

Grid convergent behavior is observed, with the difference between the fine and medium grids being over two times smaller than the difference from medium to coarse. The value of T_c is within 1% of the reference for the isolated propeller, which we consider adequate.

B. Wing Pressure Distribution

Pressure coefficient $Cp = (p - p_\infty)/q_\infty$, where p is the static pressure and p_∞ is the freestream static pressure, are computed on two planes on either side of the propeller. The two Cp cut locations, named up-going and down-going, are on planes at 70% of the propeller radius (71.12 mm), on either side of the propeller axis. We select the highest flap deflection and angle of attack in our simulations, to perform a resolution study of Cp, as this should be a challenging case and would indicate the resolution is adequate for the other cases. The results of this study are shown in Fig. 3.

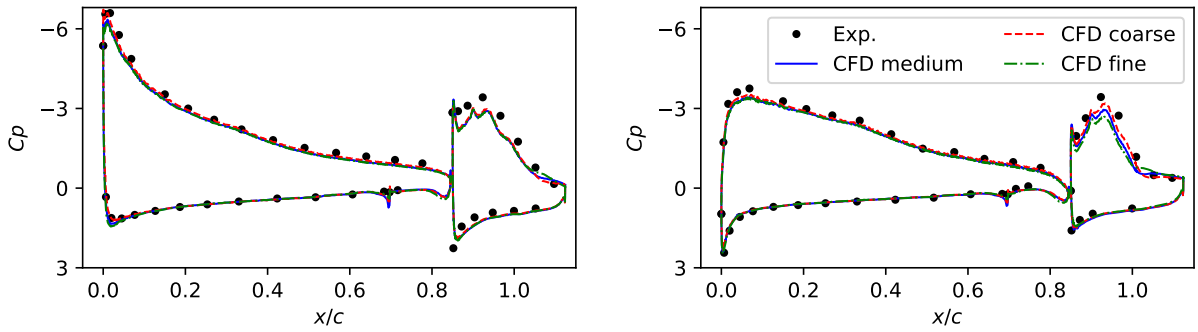

(a) Up-going wing side **(b) Down-going wing side**

Fig. 3 Effect of grid resolution on pressure coefficient along the wing chord for $\delta_f = 30°$, $\alpha = 8°$.

The smooth body separation over the flap is slightly affected by the resolution, in particular on the down-going side, but the results do not change substantially with increase in grid resolution. Hence, we use the medium resolution throughout this study.

While the main element of the wing was tripped in the experiments, the flap was not. At such low Reynolds numbers (600,000 based on the clean wing chord), substantial regions of laminar flow can occur and laminar separation bubbles were observed on the flap in the experiments. To verify the sensitivity to such effects, we conducted simulations using a transition model [27] on the flap. This made the flap leading-edge laminar and the results of this are shown in Fig. 4. The pressure cuts show a small delay in the flap separation, improving the pressure distribution on the flap, and also the suction peak on the main element of the wing. Using a more advanced transition treatment, capable of accurately capturing separation bubbles [28] could lead to further improvements.

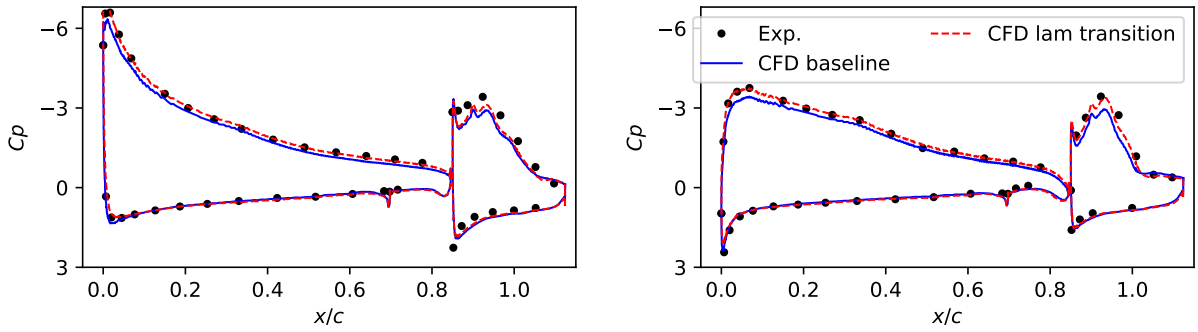

(a) Up-going wing side **(b) Down-going wing side**

Fig. 4 Effect of laminar to turbulent transition on pressure coefficient along the wing chord for $\delta_f = 30°$, $\alpha = 8°$.

Although the results with the transition model show a slight improvement over the fully turbulent simulation, the differences are small enough that we set the remaining cases to fully turbulent, to avoid any uncertainties associated with using a transition model for a high-lift configuration [29]. This also facilitates the grid resolution study, as transition models have been shown to be sensitive to the mesh [30].

Results for various values of α and δ_f can be seen in Fig. 5. All configurations results show very good agreement with experiment. As δ_f increases, the simulations show discrepancies compared to experiments in the suction peaks, which as shown in Fig. 4, is connected to laminar to turbulent transition. In all simulations the additional total pressure generated by the propeller is well captured, as the Cp values at the stagnation points agree with experimental values.

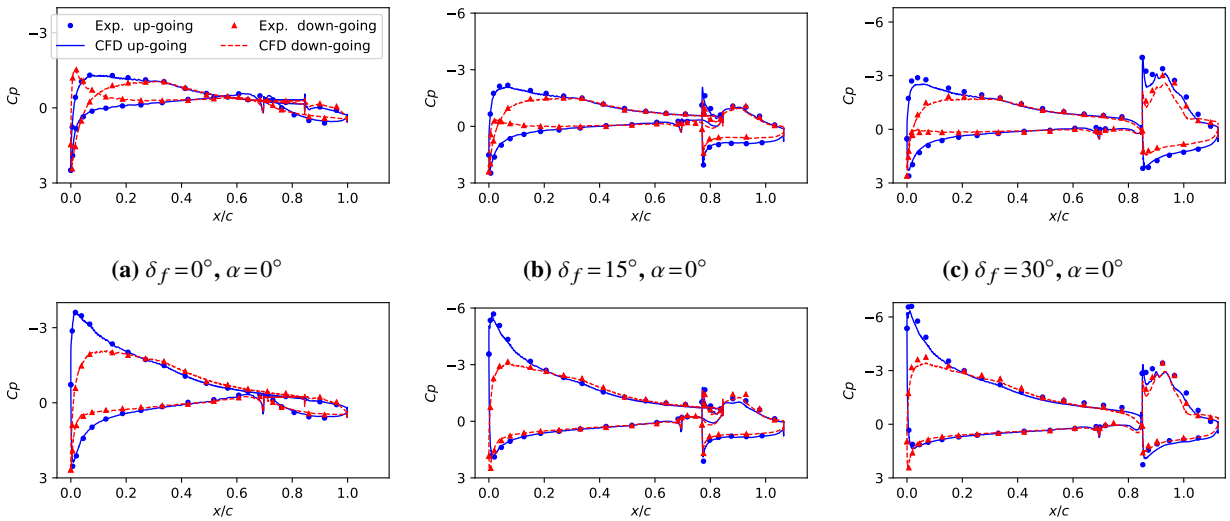

(a) $\delta_f = 0°$, $\alpha = 0°$ **(b)** $\delta_f = 15°$, $\alpha = 0°$ **(c)** $\delta_f = 30°$, $\alpha = 0°$

(d) $\delta_f = 0°$, $\alpha = 8°$ **(e)** $\delta_f = 15°$, $\alpha = 8°$ **(f)** $\delta_f = 30°$, $\alpha = 8°$

Fig. 5 Pressure coefficient along the wing chord on the up-going and down-going blade sides of the propeller for different flap angles δ_f and angles of attack α.

C. Surface Oil Flow

Oil flow measurements allow us to compare the flow features of the experiments with simulations. In particular, 3D flow separations and the footprint of the slipstream can be assessed. Top views of the experimental oil flow visualization are shown in the top rows of Figs. 6 and 7, and compared to surface shear lines from the simulations in the bottom rows. The CFD results also show streamwise shear force C_{fx}, normalized by q_∞ to assist in visualizing regions near flow separation. Note that the experimental oil flow images show some effect of gravity, turning the oil towards the up-going blade side, as the wing was mounted vertically in the wind tunnel. This effect is mostly present in areas with low surface shear.

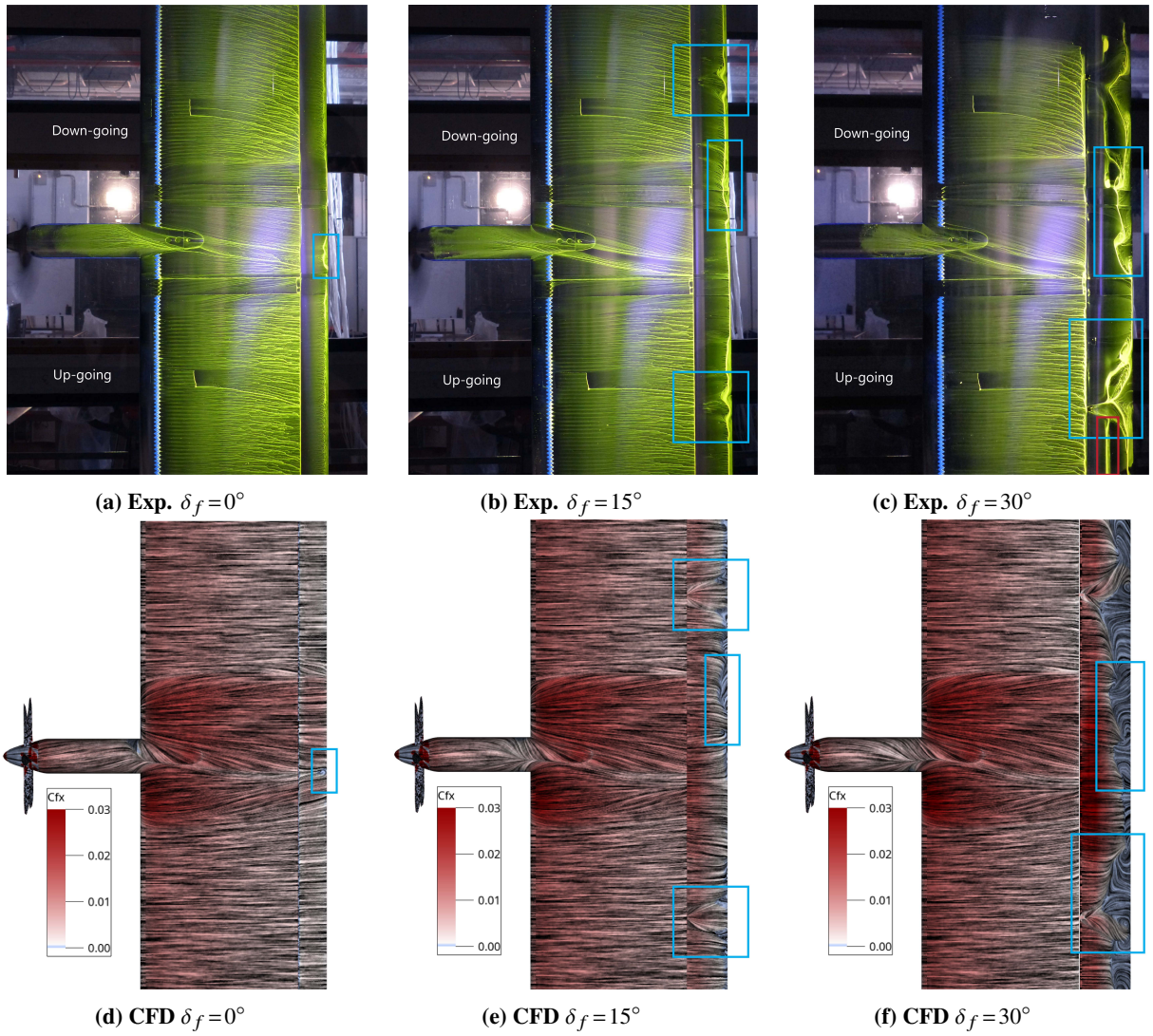

(a) Exp. $\delta_f = 0°$ **(b) Exp.** $\delta_f = 15°$ **(c) Exp.** $\delta_f = 30°$

(d) CFD $\delta_f = 0°$ **(e) CFD** $\delta_f = 15°$ **(f) CFD** $\delta_f = 30°$

Fig. 6 Surface shear lines, represented by oil flow in the experiment and colored by streamwise skin friction coefficient in simulations at $\alpha = 0°$**.**

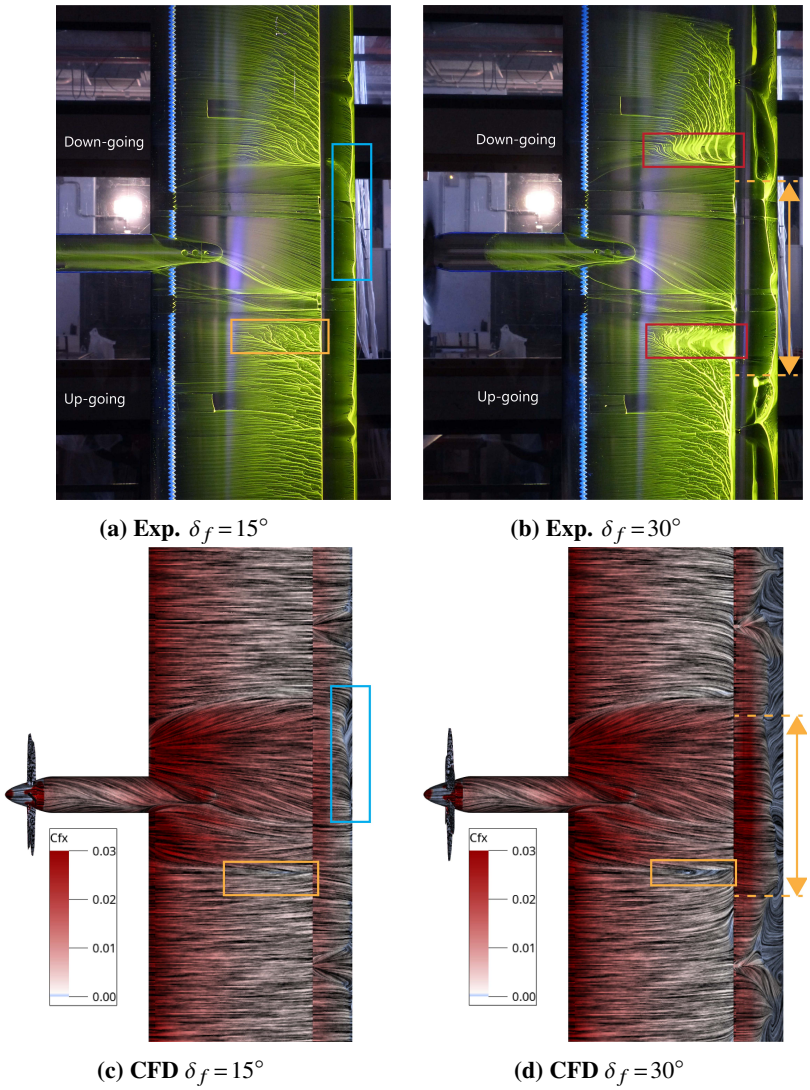

(a) Exp. $\delta_f = 15°$ **(b) Exp.** $\delta_f = 30°$

(c) CFD $\delta_f = 15°$ **(d) CFD** $\delta_f = 30°$

Fig. 7 Surface shear lines, represented by oil flow in the experiment and colored by streamwise skin friction coefficient in simulations at $\alpha = 8°$.

Figures 6 and 7 are also annotated to show specific areas of interest. Blue boxes are used to draw attention to several flow structures that match very well between the experimental oil flow and the simulated surface shear. Red boxes show differences between simulations and experiments. Figures 6a and 6d both show a slight separation due to nacelle vortex structure. With flaps deployed, the interference of the flap brackets on the flap flow is clearly visible in both experiment and simulation. The local separation on the flap is also captured well by the simulations, where the flow structures near the center of the flap span in Fig. 6c and Fig. 6f are particularly of note. They also show the presence of the laminar separation bubble on the flap (marked in red in Fig. 6c), which is not present in the simulation and has some effect on the flap separation.

At $\alpha = 8°$ (Fig. 7), the major flow structures, such as the effect of flap brackets and the crossflows directly behind the nacelle, are again captured well. The separated areas on the main element are captured by the simulation, but seem under-predicted (marked with orange boxes). They only occur on the up-going blade side in the simulation, while Fig. 7b shows clear signs of separation on the main element on the down-going blade side as well. The area of the flap that is affected by the slipstream also seems slightly larger in the oil flow images, although this cannot be fully judged from these images alone. Nonetheless, overall the simulations shear lines agree well with experimental oil flow visualization, which is very challenging to achieve in numerical simulations with smooth body separations [29].

D. Total Pressure Wake Plane

Total pressure coefficient $Cp_T = (p_T - p_\infty)/q_\infty$, where $p_T = p + q$, $q = 0.5\rho U^2$, ρ is the local air density, and U is the local velocity magnitude, is computed on a plane one chord downstream of the nested flap trailing-edge at $\alpha = 0$. Experimental results are shown on the top rows of Figs. 8 and 9, while the simulations are shown in the bottom rows. The horizontal lines represent the wing leading-edge and flap trailing-edge, while the circles indicate the propeller position.

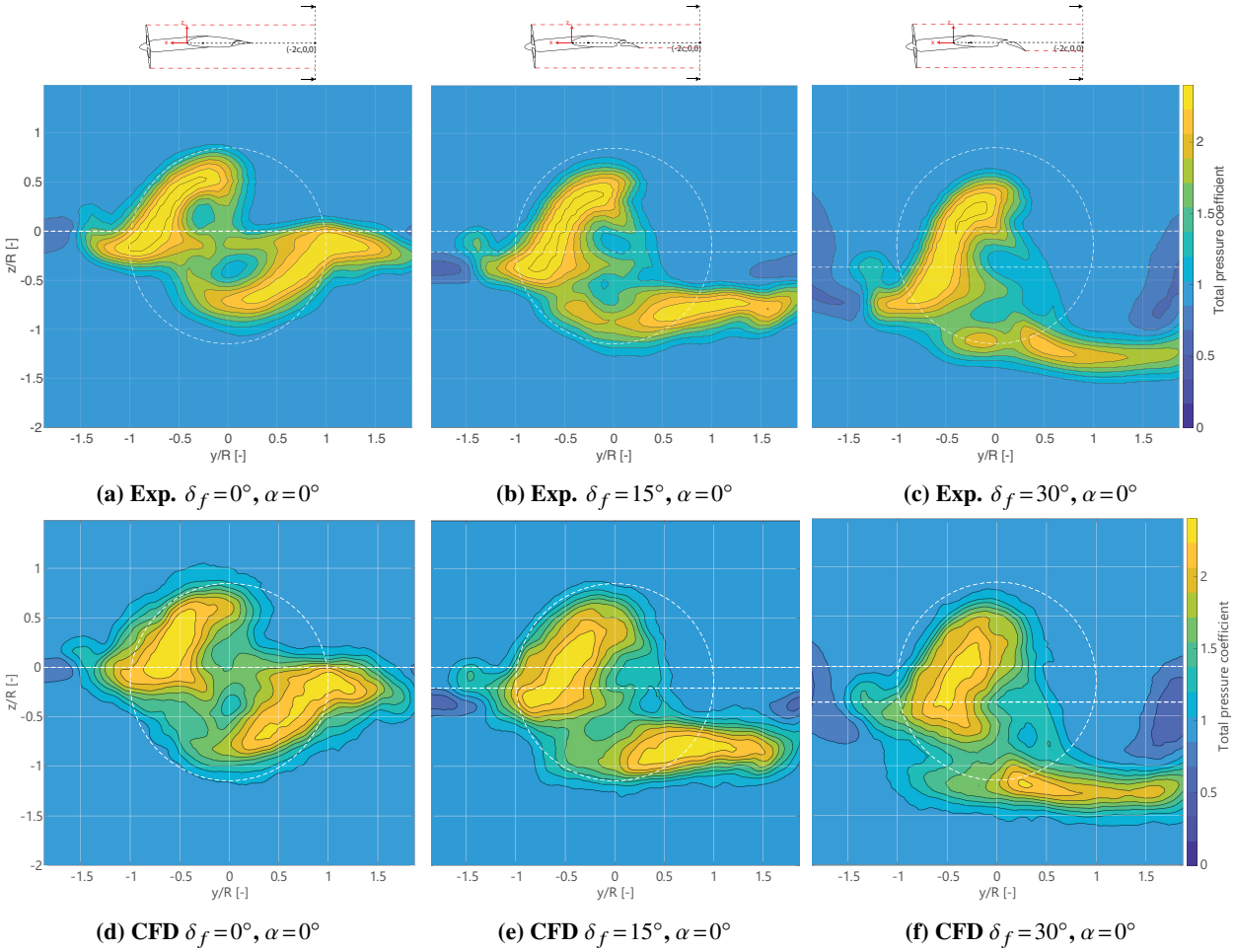

(a) Exp. $\delta_f = 0°$, $\alpha = 0°$ **(b) Exp.** $\delta_f = 15°$, $\alpha = 0°$ **(c) Exp.** $\delta_f = 30°$, $\alpha = 0°$

(d) CFD $\delta_f = 0°$, $\alpha = 0°$ **(e) CFD** $\delta_f = 15°$, $\alpha = 0°$ **(f) CFD** $\delta_f = 30°$, $\alpha = 0°$

Fig. 8 Total pressure coefficient planes in the wake of the wing.

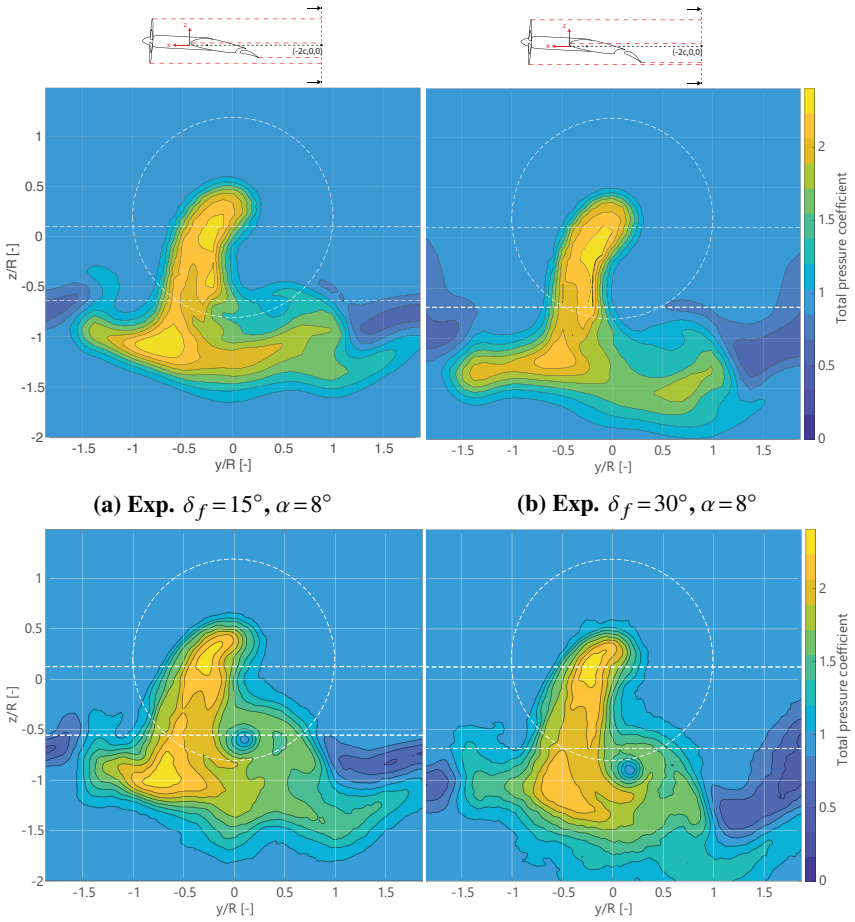

(a) Exp. $\delta_f = 15°$, $\alpha = 8°$ **(b) Exp.** $\delta_f = 30°$, $\alpha = 8°$

(c) CFD $\delta_f = 15°$, $\alpha = 8°$ **(d) CFD** $\delta_f = 30°$, $\alpha = 8°$

Fig. 9 Total pressure coefficient planes in the wake of the wing. Experimental results from [5].

The flow features of the propeller wake being cut by the wing and the slipstream on the upper surface moving to the down-going side, while the slipstream on the lower surface moves to the up-going side are well captured by the simulations. The vortices that appear as blue circles near the center of the images are also well captured, with small differences that increase with α and δ_f. The "inverted-T" shape that appears at $\alpha = 8°$ is also captured by the simulations, with some differences (at least in part) due to the slightly different flap separations. Again, overall the simulations and experiments agree well. Matching the slipstream in a downstream location such as this would be very challenging with traditional NS solvers, due to the dissipation of the tip vortices.

V. Flow Analysis

The close match of the simulations with the experimental results also offers the opportunity to use the simulations to further investigate the flow. Taking advantage of the full domain time-accurate data available from the simulation, we are able to quantify the slipstream shear and reflect on the off-the-surface structure of the slipstream.

A. On-the-surface slipstream trajectory

Figure 10 shows the spanwise distribution of skin friction coefficient $Cf = F/q_\infty$, where F is the amplitude of the force vector acting on the wing surface, on the main element of the wing for different chordwise stations. Solid lines correspond to the upper surface of the wing, while dashed lines show the same station on the lower surface. Positive y/R corresponds to the down-going blade side. The slipstream edges, highlighted with markers, can be identified from the substantial change in skin friction due to the presence of the slipstream. Plotting the positions of the markers in Fig. 10 illustrates the on-the-surface translation of the slipstream edge as it moves along the wing. This is shown in Fig. 11.

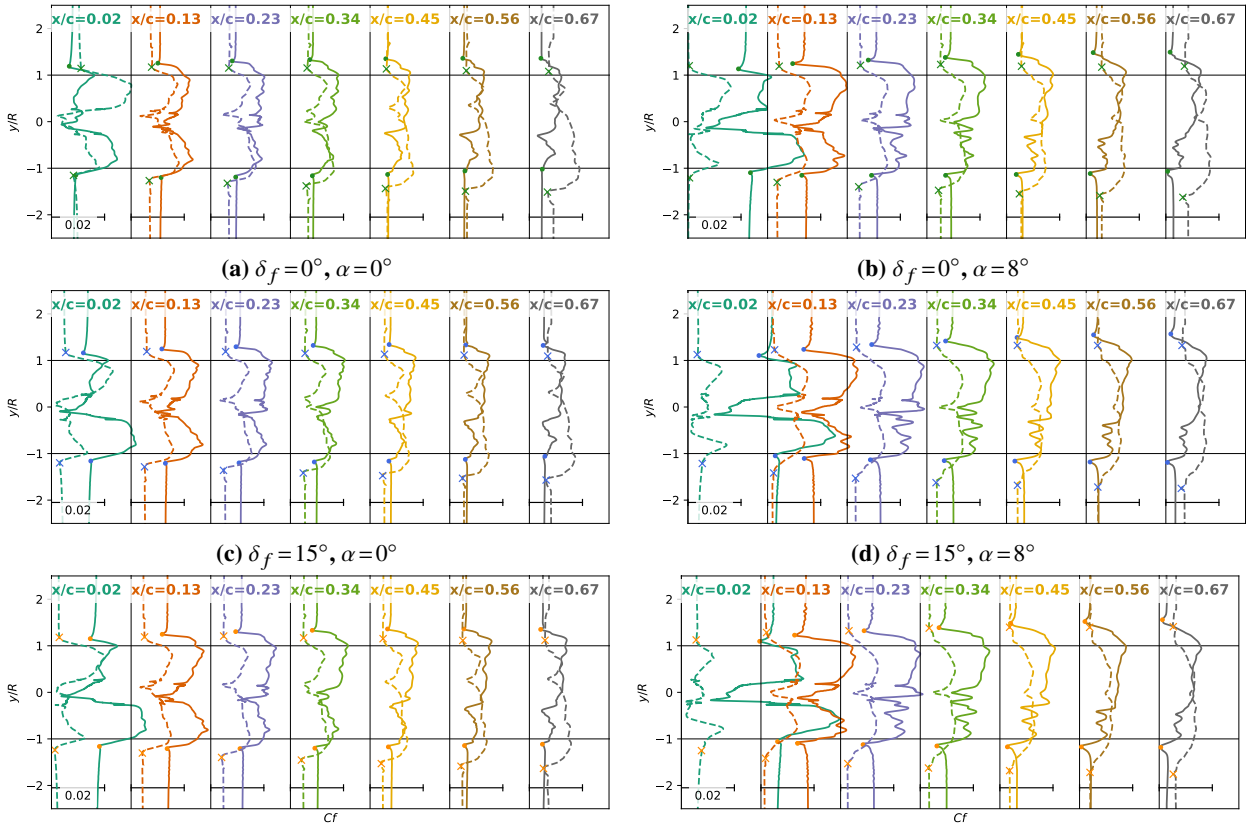

(a) $\delta_f = 0°$, $\alpha = 0°$ **(b)** $\delta_f = 0°$, $\alpha = 8°$

(c) $\delta_f = 15°$, $\alpha = 0°$ **(d)** $\delta_f = 15°$, $\alpha = 8°$

(e) $\delta_f = 30°$, $\alpha = 0°$ **(f)** $\delta_f = 30°$, $\alpha = 8°$

Fig. 10 Spanwise skin friction distributions for various chordwise positions. Dashed lines are on the lower surface of the wing, solid lines are on the upper surface. Markers show the approximate edges of the slipstreams. Marker colors correspond to the lines in Fig. 11

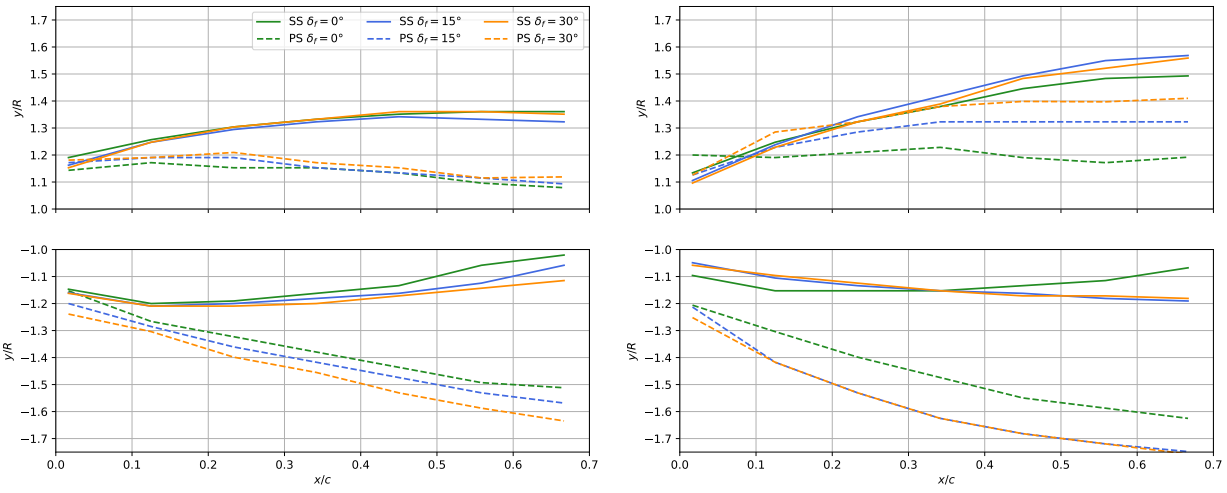

(a) $\alpha = 0°$ **(b)** $\alpha = 8°$

Fig. 11 Spanwise evolution of propeller wake size on wing. Solid lines represent the suction side (SS) of the wing, dashed lines the pressure side (PS).

Several observations are shared between all configurations. Close to the leading-edge of the wing the slipstream-affected area is slightly wider for $\alpha = 0°$ than for $\alpha = 8$. This is caused by the different trajectory of the slipstream between disk and wing leading-edge due to the angle of attack. At $\alpha = 8°$ the wing intersects the slipstream at a lower part, where the slipstream is less wide. We can also see that the slipstream-affected area is generally wider than one propeller diameter at $x/c = 0.02$. This is a function of the balance between propeller thrust coefficient (and associated slipstream contraction) and the nacelle width (and associated slipstream displacement). Furthermore, it depends on the intersection position of the wing as a result of propeller position, inclination, and wing angle of attack.

For all presented cases, we can see a slight divergence of the slipstream affected area between $x/c = 0.02$ and $x/c = 0.13$. This is particularly apparent on the upper surface. This leading-edge expansion is also noted in the experiment by Duivenvoorden et al. [5]. We attribute this to a vortex imaging effect of the tip vortices bending around the leading-edge, which is also described by Thom [31]. Rather than being cut at the leading-edge, as suggested by Veldhuis [32], the tip vortex remains intact and stretches around the wing leading-edge. This is clearly visible in Fig. 12 and follows experimental flow visualisations of propeller-rudder interaction performed by Felli et al. [33, 34]. Due to image vortex effects on the wing surface, this tip vortex will self-induce away from the centerline. As the tip vortices move downstream, the stretched portion loses strength of even disintegrates and the expansion effect disappears.

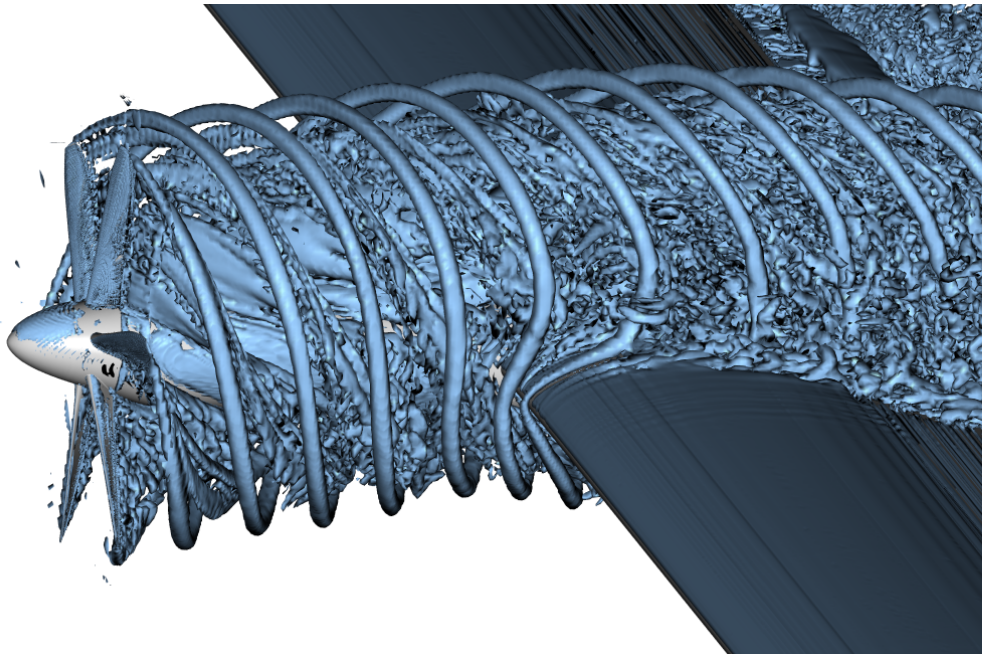

Fig. 12 Isosurfaces of instantaneous $\lambda_2 = -5U_\infty^2/c^2$ for $\delta_f = 30°$, $\alpha = 8°$, showing the tip vortex wrapping around the leading-edge.

Figure 11 also clearly illustrates the shearing effect between the slipstream portions passing either side of the wing and how this effect is compounded with other factors. On the up-going blade side, the lower surface slipstream edge clearly moves away from the propeller axis, while the upper surface slipstream edge moves toward the axis, but to a lesser extent due to the shear being counteracted by the initial leading-edge expansion. On the down-going blade side, the upper surface slipstream edge clearly moves away from the axis, while the lower surface moves very little. As the slipstream moves downstream on the wing, the slipstream edge on the down-going blade side of the lower surface becomes difficult to distinguish exactly. The amount of shear clearly increases at higher α.

Deploying the flap and increasing angle of attack both show to have an expansion effect on the slipstream, most evident from the upper surface up-going blade side slipstream edge. Figures 10a, 10c, 10e and 10b all clearly show an initial movement away from the axis between $x/c = 0.02$ and $x/c = 0.13$, followed by movement towards the axis up to $x/c = 0.67$. For Figs. 10d and 10f the latter no long occurs and the slipstream edge continues to move away slightly. Overall, the slipstream thus both shears and expands as it moves over the main element.

Finally, the skin friction coefficient distributions in Fig. 10 show that increasing both angle of attack and flap deflection cause the effect of the slipstream on the lower surface skin friction to become dissipated. We attribute this

to the effect of interactions between tip vortices on the slipstream development and the dependency on slipstream deflection.

B. Tip vortex interaction

Figure 13 shows side views of the vortical slipstream structures as they pass the wing for various angles of attack and flap deflections. In Fig. 13a the tip vortices initially remain concentrated, but start to interact around the wing mid-chord and break down into larger structures by the time the slipstream reaches the trailing-edge. Increasing the angle of attack increases the wing circulation, thus increasing velocity on the upper side and maintaining separate flow structures further downstream. On the lower side, the flow decelerates, causing tip vortices to interact sooner. This is similar to the effect of increasing the number of blades [35] or decreasing the advance ratio.

Deploying the flap has a similar effect. Distinct tip vortex structures are maintained further downstream on the upper side and on the lower side interaction occurs further upstream. With the addition of increased angle of attack these effects are amplified, inducing tip vortex interactions nearly at the leading-edge of the lower side. As no concentrated tip vortices reach the flap, the interaction of the slipstream with the flap will be different from the main element. For instance, there will be no stretching of the vortex leading to self-induced expansion.

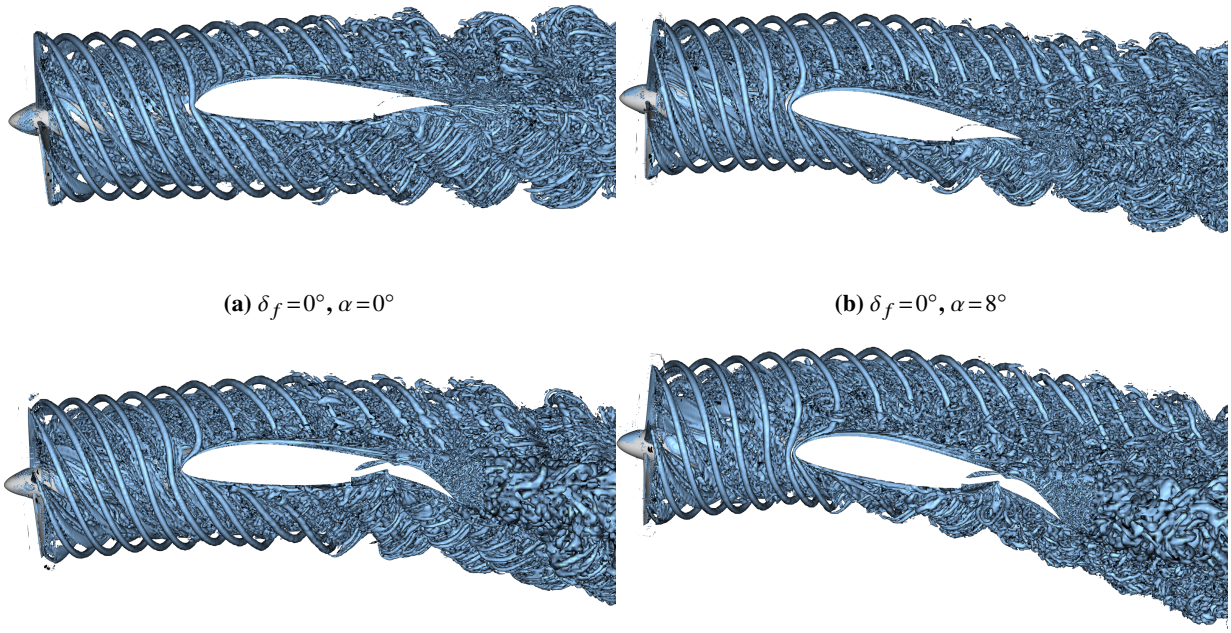

(a) $\delta_f = 0°$, $\alpha = 0°$ **(b)** $\delta_f = 0°$, $\alpha = 8°$

(c) $\delta_f = 30°$, $\alpha = 0°$ **(d)** $\delta_f = 30°$, $\alpha = 8°$

Fig. 13 Isosurfaces of instantaneous $\lambda_2 = -5U_\infty^2/c^2$, illustrating how angle of attack and flap deflection affect slipstream evolution and instability.

C. Slipstream deformation

Both the skin friction distributions of Fig. 10 and the tip vortex interactions shown in Fig. 13 show how much the slipstream shape is distorted as it passes over the wing. The "inverted-T" shape of the slipstream in the wing wake starts developing early on the wing, not just in the wake of the wing. This is visualized in Fig. 14a, showing slices of the total pressure coefficient Cp_T at various streamwise positions for the case with $\delta_f = 15°$ and $\alpha = 8°$. Only $Cp_T > 1.2$ is visualized to highlight the slipstream. The figure clearly shows that the "inverted-T" shape is the result of deformation across the entire wing chord. The stem of this "T" develops from a minor deformation at the wing leading-edge, combined with contraction of the slipstream. The lower half expands significantly, likely due to the spanwise pressure gradient and the tip vortex interactions and associated break-down.

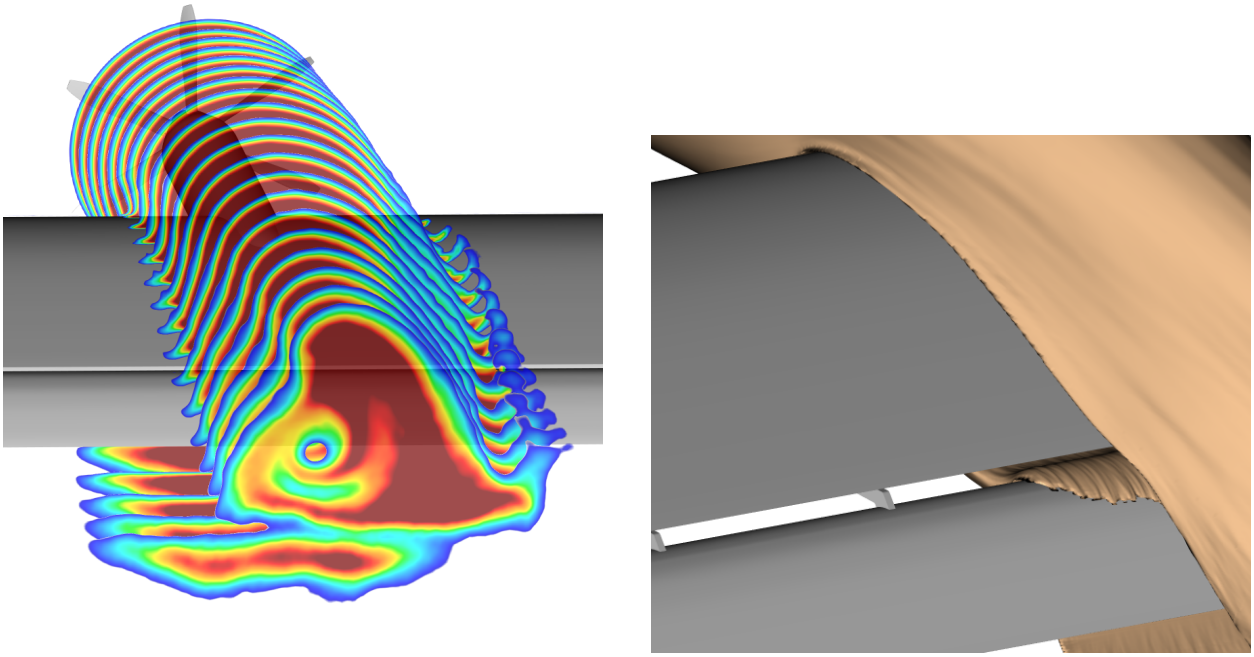

(a) Slices of total pressure coefficient (>1.2), **(b) Isosurfaces of $C_{p,T} = 1.2$,**

Fig. 14 Visualisation of the slipstream deformation as it moves along the wing based on (time-averaged) total pressure coefficient $C_{p,T}$ for the $\delta_f = 15°$, $\alpha = 8°$ case.

The extent of the shearing effect of both slipstream halves as they pass the wing is also clearly visualized in Fig. 14a. The flap thus encounters very different flows depending on the spanwise station. This varies from being only immersed in the portion of the slipstream that passes the lower half of the main element to being fully immersed in the slipstream or only having the slipstream pass it off-the-surface. For most spanwise stations, the total pressure varies strongly in the vertical direction. By taking an isosurface of the mean total pressure, shown in Fig. 14b, we can also see that a portion of the slipstream will pass through the slot and over the flap suction surface.

VI. Conclusions and Outlook

The conclusions we can draw from this work are:

- LBM simulations show very good agreement with experimental measurements on both qualitative and quantitative aspects.
- Wake development is captured to an impressive level considering the usual difficulty of numerical methods with numerical dissipation and diffusion.
- Quantification of the slipstream edge trajectory showed a combination of shearing and expanding effects, the balance of which dictates spanwise variation of flow on the flap.
- Slipstream trajectory change due to angle of attack can have a significant effect on the spanwise area of the wing that intersects the slipstream.
- Tip vortices are stretched around the leading-edge rather than cut by it, leading to slipstream expansion through image vortex mechanisms.
- Angle of attack and flap deflection have significant effect on tip vortex evolution by affecting vortex-vortex interactions, leading to instabilities.

Future work will focus on further analysis of slipstream deformation and flap interaction, potentially including multiple propellers.

References

[1] Deere, K. A., Viken, J. K., Viken, S., Carter, M. B., Wiese, M., and Farr, N., "Computational Analysis of a Wing Designed for the X-57 Distributed Electric Propulsion Aircraft," *35th AIAA Applied Aerodynamics Conference*, 2017. https://doi.org/10.2514/6.2017-3923.

[2] Sinnige, T., Nederlof, R., and van Arnhem, N., "Aerodynamic Performance of Wingtip-Mounted Propellers in Tractor and Pusher Configuration," *AIAA AVIATION FORUM*, 2021. https://doi.org/10.2514/6.2021-2511.

[3] Stokkermans, T. C. A., Usai, D., Sinnige, T., and Veldhuis, L. L. M., "Aerodynamic Interaction Effects Between Propellers in Typical eVTOL Vehicle Configurations," *Journal of Aircraft*, Vol. 58, No. 4, 2021, pp. 815–833. https://doi.org/10.2514/1.C035814.

[4] de Vries, R., van Arnhem, N., Sinnige, T., Vos, R., and Veldhuis, L. L., "Aerodynamic interaction between propellers of a distributed-propulsion system in forward flight," *Aerospace Science and Technology*, Vol. 118, 2021, p. 107009. https://doi.org/10.1016/j.ast.2021.107009.

[5] Duivenvoorden, R. R., Suard, N., Sinnige, T., and Veldhuis, L. L. M., "Experimental Investigation of Aerodynamic Interactions of a Wing with Deployed Fowler Flap under Influence of a Propeller Slipstream," *AIAA AVIATION Forum*, 2022. https://doi.org/10.2514/6.2022-3216.

[6] Chen, H., Teixeira, C., and Molvig, K., "Digital Physics Approach to Computational Fluid Dynamics: Some Basic Theoretical Features," *International Journal of Modern Physics C*, Vol. 08, No. 04, 1997, pp. 675–684. https://doi.org/10.1142/S0129183197000576.

[7] Chen, H., Chen, S., and Matthaeus, W. H., "Recovery of the Navier-Stokes equations using a lattice-gas Boltzmann method," *Phys. Rev. A*, Vol. 45, 1992, pp. R5339–R5342. https://doi.org/10.1103/PhysRevA.45.R5339.

[8] Brès, G., Pérot, F., and Freed, D., "Properties of the Lattice Boltzmann Method for Acoustics," *15th AIAA/CEAS Aeroacoustics Conference (30th AIAA Aeroacoustics Conference)*, 2012. https://doi.org/10.2514/6.2009-3395.

[9] Manoha, E., and Caruelle, B., "Summary of the LAGOON Solutions from the Benchmark problems for Airframe Noise Computations-III Workshop," *21st AIAA/CEAS Aeroacoustics Conference*, 2015. https://doi.org/10.2514/6.2015-2846.

[10] Succi, S., *The Lattice Boltzmann Equation: For Fluid Dynamics and Beyond*, Clarendon Press, 2001. URL https://books.google.com/books?id=OC0Sj_xgnhAC.

[11] Bhatnagar, P. L., Gross, E. P., and Krook, M., "A Model for Collision Processes in Gases. I. Small Amplitude Processes in Charged and Neutral One-Component Systems," *Physical Review*, Vol. 94, 1954, pp. 511–525. https://doi.org/10.1103/PhysRev.94.511.

[12] Yakhot, V., Orszag, S. A., Thangam, S., Gatski, T. B., and Speziale, C. G., "Development of turbulence models for shear flows by a double expansion technique," *Physics of Fluids A: Fluid Dynamics*, Vol. 4, No. 7, 1992, pp. 1510–1520. https://doi.org/10.1063/1.858424.

[13] Fares, E., Duda, B., Ribeiro, A. F. P., and König, B., "Scale-resolving simulations using a lattice Boltzmann-based approach," *CEAS Aeronautical Journal*, Vol. 9, No. 4, 2018. https://doi.org/10.1007/s13272-018-0317-0.

[14] Khorrami, M. R., Konig, B., Fares, E., Ribeiro, A., Czech, M., and Ravetta, P. A., "Airframe Noise Simulations of a Full-Scale Large Civil Transport in Landing Configuration," *AIAA AVIATION FORUM*, 2021. https://doi.org/10.2514/6.2021-2161.

[15] Chen, H., Teixeira, C., and Molvig, K., "Realization of Fluid Boundary Conditions via Discrete Boltzmann Dynamics," *International Journal of Modern Physics C*, Vol. 09, No. 08, 1998, pp. 1281–1292. https://doi.org/10.1142/S0129183198001151.

[16] Zhang, R., Sun, C., Li, Y., Satti, R., Shock, R., Hoch, J., and Chen, H., "Lattice Boltzmann Approach for Local Reference Frames," *Communications in Computational Physics*, Vol. 9, No. 5, 2011, p. 1193–1205. https://doi.org/10.4208/cicp.021109.111110s.

[17] Ribeiro, A. F. P., "Unsteady Analysis of Ground Vortex Ingestion with LBM-VLES," *AIAA SCITECH Forum*, 2021. https://doi.org/10.2514/6.2022-0224.

[18] Casalino, D., van der Velden, W. C., and Romani, G., "A Framework for Multi-Fidelity Wind-Turbine Aeroacoustic Simulations," *28th AIAA/CEAS Aeroacoustics 2022 Conference*, 2022. https://doi.org/10.2514/6.2022-2892.

[19] Ribeiro, A. F. P., Murayama, M., Ito, Y., Yamamoto, K., and Hirai, T., "Effect of Slat Tracks and Inboard Slat Tip Geometry on Airframe Noise," 2022. https://doi.org/10.2514/6.2022-2952.

[20] König, B., Singh, D., Ribeiro, A., and Fares, E., "Lattice-Boltzmann Simulations at the Corners of the Flight Envelope," *54th 3AF International Conference on Applied Aerodynamics*, 2019.

[21] Lucas-Bodas, S. D., Narbona-Gonzalez, J., Ossorio-Contreras, V., Jose, J., Guerra-Crespo, Funes-Sebastian, D. E., and Ruiz-Calavera, L. P., "Experimental Validation of Numerical Prediction of Wing-Propeller Aerodynamic Interaction," *32nd Congress of the International Council of the Aeronautical Sciences*, 2021. URL https://www.icas.org/ICAS_ARCHIVE/ICAS2020/data/papers/ICAS2020_0171_paper.pdf.

[22] Boermans, L., and Rutten, P., "Two-dimensional aerodynamic characteristics of airfoil NLF-MOD22 with fowler flap," Technical report, Delft University of Technology, 1995.

[23] van Arnhem, N., de Vries, R., Sinnige, T., and Veldhuis, L., "TUD-XPROP-S propeller geometry," , Mar. 2022. https://doi.org/10.5281/zenodo.6355670.

[24] Ribeiro, A. F. P., Casalino, D., and Fares, E., "Lattice-Boltzmann Simulations of an Oscillating NACA0012 Airfoil in Dynamic Stall," *Advances in Fluid-Structure Interaction*, edited by M. Braza, A. Bottaro, and M. Thompson, Springer International Publishing, 2016, pp. 179–192.

[25] Ribeiro, A. F. P., Singh, D., Konig, B., and Fares, E., "On the Stall Characteristics of Iced Wings," *55th AIAA Aerospace Sciences Meeting*, 2017. https://doi.org/10.2514/6.2017-1426.

[26] Konig, B., Duda, B. M., and Laskowski, G. M., "Lattice Boltzmann Simulations for the 4th AIAA High-Lift Prediction Workshop using PowerFLOW," 2022. https://doi.org/10.2514/6.2022-3433.

[27] Duda, B. M., Fares, E., Kotapati, R., Li, Y., Staroselsky, I., Zhang, R., and Chen, H., "Capturing Laminar to Turbulent Transition within the LBM based CFD solver PowerFLOW," *AIAA Scitech Forum*, 2019. https://doi.org/10.2514/6.2019-1832.

[28] Casalino, D., Romani, G., Zhang, R., and Chen, H., "Lattice-Boltzmann calculations of rotor aeroacoustics in transitional boundary layer regime," *Aerospace Science and Technology*, Vol. 130, 2022, p. 107953. https://doi.org/10.1016/j.ast.2022.107953.

[29] Rumsey, C. L., Slotnick, J. P., and Sclafani, A. J., "Overview and Summary of the Third AIAA High Lift Prediction Workshop," *Journal of Aircraft*, Vol. 56, No. 2, 2019, pp. 621–644. https://doi.org/10.2514/1.C034940.

[30] Carnes, J., and Coder, J. G., "Benchmarking the Langtry-Menter Transition Model Using OVERFLOW for the AIAA Transition Modeling Workshop," *AIAA AVIATION Forum*, 2022. https://doi.org/10.2514/6.2022-3680.

[31] Thom, A. D., "Analysis of Vortex-Lifting Surface Interactions," PhD dissertation, 2011. URL http://theses.gla.ac.uk/3037/1/2011thomphd.pdf.

[32] Veldhuis, L., "Propeller wing aerodynamic interference," PhD dissertation, Delft University of Technology, 2005. URL http://www.narcis.nl/publication/RecordID/oai:tudelft.nl:uuid:8ffbde9c-b483-40de-90e0-97095202fbe3.

[33] Felli, M., Di Felice, F., Guj, G., and Camussi, R., "Analysis of the propeller wake evolution by pressure and velocity phase measurements," *Experiments in Fluids*, Vol. 41, No. 3, 2006, pp. 441–451. https://doi.org/10.1007/s00348-006-0171-4.

[34] Felli, M., and Falchi, M., "Propeller tip and hub vortex dynamics in the interaction with a rudder," *Experiments in Fluids*, Vol. 51, No. 5, 2011, pp. 1385–1402. https://doi.org/10.1007/s00348-011-1162-7.

[35] Felli, M., Guj, G., and Camussi, R., "Effect of the number of blades on propeller wake evolution," *Experiments in Fluids*, Vol. 44, 2008, pp. 409–418. https://doi.org/10.1007/s00348-007-0385-0.